Chemical Engineering Journal 161 (2010) 257–268

Contents lists available at ScienceDirect

Chemical Engineering Journal

journal homepage: www.elsevier.com/locate/cej

CFD study of an evaporative trickle bed reactor: Mal-distribution and thermal runaway induced by feed disturbances

Wayne Strasser*

Eastman Chemical Company, PO Box 511, Kingsport, TN 37662, USA

ARTICLE INFO

Article history:
Received 5 February 2010
Received in revised form 26 April 2010
Accepted 27 April 2010

Keywords:
Heat transfer
Multiphase reactors
Porous media
Numerical analysis
Transport processes
Reaction engineering

ABSTRACT

A numerical study was carried out to investigate steady-state and transient phase distribution, evaporation, and thermal runaway in a large-scale high-pressure trickle bed reactor. A cooling recycle stream, containing reaction products and a fresh feed, was included via a closed loop calculation. It was found that, as expected, phase distribution in the catalyst bed had a substantial impact on production rate; a faulty feed distribution system can cost approximately 20% in overall steady-state product conversion. In the event that the cooling recycle stream is lost, the external reactor shell temperature can exceed its design intent. It was found that reducing the quantity of fresh reactant feed in this situation can dramatically reduce the potential for vessel damage. Thermal inertia of the catalyst particles proved to be a significant contribution to the transient energy balance. Model results are supported with a posteriori thermal excursion plant data.

1. Introduction

A plug-flow adiabatic vertical tubular reactor is often used to perform a hydrogenation process (HDP) at high pressures (>100 bar), as is the case in the present work (Fig. 1). Unsaturated hydrocarbons (UNSAT), along with a solvent, are fed to the top of the reactor. Hydrogen is fed co-currently with the liquid. Below the feed distribution system is a bed of ceramic catalyst particles. As the UNSAT, solvent, and hydrogen trickle their way through the catalyst bed, the saturation of the hydrocarbons is increased and is converted to a saturated (SAT) species. There is also mass, momentum, and energy transferred among the fluid phases, catalyst bed particles, and reactor shell. In addition to evaporation/condensation, there is a high percentage of mass (>95%) consumed from the gas phase. An overly simplified, unbalanced sample reaction is shown in Eq (1) below. The kinetic rate expression is purposely undisclosed, but it can be said that it is temperature and pressure dependent.

$$H_2 + \text{UNSAT} = \text{SAT} \quad (1)$$

The reaction is highly exothermic, so an external cooling loop is provided. That is, a recycle stream is cooled externally and is then combined with the fresh liquid feed at the inlet. Liquid reactant mal-distribution causes a number of problems. First, the catalyst system would be underutilized. This would lead to premature and non-uniform catalyst deactivation according to Lopes and Quinta-Ferreira [1]. Second, local "hot-spots" might surface in areas of low liquid wetting as noted by and Lopes and Quinta-Ferreira [1] and Gunjal and Ranade [2]; however, the present reaction system constrains the system even further: reactor shell damage could occur if the primary source of temperature control, the cooled recycle stream, is temporarily lost.

2. Previous work

A thorough review of trickle bed reactor (TBR) hydrodynamics is given by Al-Dahhan et al. [3]. In short, TBRs typically have two main categories of flow conditions: low interaction regime (LIR) and high interaction regime (HIR). LIR occurs when there are relatively low flows of gas and liquid. The liquid flow is mainly gravity-driven, and there are weak gas–liquid interfacial effects. At higher flow rates of both phases, there is intense gas–liquid shear. Various HIR flow patterns can result, depending on the ratio of the flows of the two phases. These patterns range from liquid-continuous at low gas flows to gas-continuous at high gas flows. At some point, there is a transition from trickle flow to pulsing flow. In the LIR, pressure has little effect on bed hydrodynamics. Table 1 shows typical parameters of the TBRs in the present work based on the calculations of Al-Dahhan et al. [3]. It can be surmised that said TBR operates in the trickling regime, specifically the LIR. Gas average mass fluxes are on the order of 0.01 kg/m^2 s; liquid fluxes are closer to 10 kg/m^2 s with recycle on and 1 kg/m^2 s when recycle is shut off. Various catalyst systems require different feed conditions and/or different relative rates of gas and liquid, yet Table 1 can

* Tel.: +1 423 229 3757; fax: +1 423 224 0453.
E-mail address: strasser@eastman.com.

1385-8947/$ – see front matter © 2010 Elsevier B.V. All rights reserved.
doi:10.1016/j.cej.2010.04.049

Nomenclature

A	drag coefficient
C	constant pressure heat capacity (J/kg K)
d	catalyst bed particle diameter (m)
D	molecular diffusivity (m^2)
F	FORTRAN-related energy sources (J/s)
g	gravity (m/s^2)
H	thermal conductivity (J/s m K)
I	inertial resistance factor (m^{-1})
k	turbulence kinetic energy (m^2/s^2)
K	area porosity
L	liquid–gas interfacial length scale (m)
M	interfacial forces (drag and non-drag) ($kg/m^2\ s^2$)
NUFS	Nusselt number for fluid–solid heat transfer
NUGL	Nusselt number for gas–liquid heat transfer
p	pressure (Pa)
P	Permeability (m^2)
Pr	liquid phase Prandtl number
r	volume fraction of phase α
R	species reaction rate (kg/m^3 s)
REGL	liquid phase slip Reynolds number
REFS	liquid phase Reynolds number
S	sources for evaporation/condensation (kg/m^3 s)
Sc	Schmidt number
t	time (s)
T	static temperature (K)
u	velocity (true, not superficial) component (m/s)
x	space coordinate (m)
Z	porous resistance ($kg/m^2\ s^2$)

Greek letters

Φ	species mass fraction
α	phase designation
δ	Kronecker delta
ε	turbulence dissipation rate (m^2/s^3)
γ	volume porosity
θ	liquid–gas interfacial area (m^{-1})
ρ	density (kg/m^3)
λ	latent heat (J/kg)
μ	viscosity (kg/m s)
ξ	heat of reaction (J/kg s)
ω	specific dissipation rate (s^{-1})

Subscripts and superscripts

$i...m$	tensor indices
t	turbulent
$'$	fluctuating component
G	gas
L	liquid

be used to help with regime identification (Charpentier and Favier [4]).

Eulerian–Eulerian (E–E) CFD approaches have been used to study fixed-bed reactors. Examples can be found in Jiang et al. [5], Jiang et al. [6], Lopes and Quinta-Ferreira [1], Lopes and Quinta-Ferreira [7], Lopes and Quinta-Ferreira [8], Gunjal and Ranade [2], and Lappalainen et al. [9]. Table 2 summarizes said work. 2DA refers to a two-dimensional axi-symmetric method. Few researchers model individual catalyst particles; most use a porous medium (PM) approach, showing it to be a useful strategy and require a much less computationally intense effort. PM studies typically involved two-dimensional domains. Lappalainen et al. [9] found that capillary dispersion is as important as mechanical dispersion

Table 1
Some typical dimensionless parameters during normal bed operation.

Superficial Weber number	8.18E−02
Superficial Reynolds number	8.17E+01
Superficial Bond number	9.25E+00
Superficial Capillary number	1.00E−03
Modified Lockhart–Martinelli ratio	6.95E−03
Charpentier x-axis parameter	4.55E−02
Charpentier y-axis parameter	2.26E+02

over a range of conditions and that the choice of porosity function affects this result. Porosity spatial variation is also explored in Jiang et al. [6]. Lopes and Quinta-Ferreira [8] found that the dispersed phase standard k–ε model was better than the RSM equivalent when individual catalyst particles are modeled. An informative comparison of volume of fluid (VOF) and E–E CFD methodologies involving individual modeled catalyst particles is given by Lopes and Quinta-Ferreira [1]. It was shown that, because of the formulation of E–E interaction terms, the VOF method (no interaction terms) was a worse predictor of hydrodynamics responses. Local liquid holdup inefficiencies were exacerbated by the VOF approach; more spatial temperature variations and hot-spots occurred with the VOF solver. Kinetics effects are considered by Gunjal and Ranade [2] and Lopes and Quinta-Ferreira [7]. In these two works, it does not appear that there is consumption of the gas phase; the only hydrodynamic effect that is influenced by kinetics appears to be the temperature-dependent properties in Gunjal and Ranade [2]. A mass transfer-related study was that of Gunjal and Ranade [2] in which gas-phase solubility in the liquid phase is incorporated, i.e. no bulk evaporation. Feed mal-distribution was studied by Lappalainen et al. [9] in two dimensions and found the porosity formulation important. Mal-distribution was also studied in 2-D by Jiang et al. [5]. They showed that feed flow temporal modulation helped to improve the holdup uniformity. There have been no CFD studies that the author is aware of involving thermal runaway, an external recycle loop, or 3-D feed-induced mal-distribution. Also, strong coupling between kinetics and hydrodynamics appears to be absent from said CFD-based TBR studies.

3. Present work

It is necessary to develop a predictive tool to explore the sample space for some design concepts, as well as mitigate thermal runaway for the reactor configuration shown in Fig. 1. Thermal runaway/draining, coupled with the strong interdependency of hydrodynamics with kinetics, evaporation, phase properties, 4-phase conjugate heat transfer, and gas consumption (>95% con-

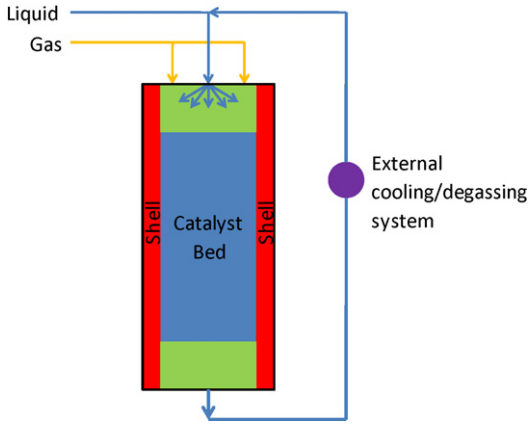

Fig. 1. Process schematic.

Table 2
Summary of some recent CFD-based TBR studies.

Authors	Year	Primary goal	Solver	Dim.	Feed	Bed	Porosity	Turbulence model	Surface forces	Trans./Drain	Heat transfer	Rxns	Recycle loop	Gas consumption	Mass transfer
Jiang et al.	2001	Bench-scale hydro.	E–E	2	Uni.	PM	f(r,z)	None	Yes	Yes	No	No	No	No	No
Jiang et al.	2002	*k*-fluid approach details	E–E	2	Uni.	PM	f(r,z)	None	Yes	Yes	No	No	No	No	No
Gunjal and Ranade	2007	Hydro-processing scales	E–E	2DA	Uni.	PM	f(r)	None	No	No	Yes	Yes	No	No	Sol.
Lopes and Quinta-Ferreira	2007	TOC conversion study	E–E	3	Uni.	Part.	N/A	skε	No	No	Yes	Yes	No	No	No
Lappalainen et al.	2009	Dispersion mechanisms	E–E	2DA	Point	PM	pdf	Disp.	Yes	No	No	No	No	No	No
Lopes and Quinta-Ferreira	2009	Turbulence models	E–E	3	Uni.	Part.	N/A	Var.	No	No	No	No	No	No	No
Lopes and Quinta-Ferreira	2010	Phase tracking	E–E/VOF	3	Uni.	Part.	N/A	sks	No	No	Yes	Yes	No	No	No
Present work	N/A	Runaway with feed loss	E–E	3	Var.	PM	Const.	SST	No	Yes	CHT	Yes	Yes	Yes	Evap.

Fig. 2. Layout of the simple model and close-up of meshes used.

sumed) make this study relevant. Also, the existence of a closed loop external recycle stream and 3-D mal-distribution, add to the industrial value of this work.

The overall purpose of this work is to prepare for the construction of a larger scale reactor (>1 m diameter) than is currently in use by the sponsor. There are multiple goals with this study. First, there is a desire to study steady-state conversion and temperature profile (liquid, gas, catalyst, and reactor shell) with two different catalyst systems and three simple feed distributors. Second, safety analyses are carried out. The goal is to investigate the thermal runaway condition in the event that the external cooling loop is lost. When this occurs, the inner wall temperature can dramatically increase, creating a situation in which the allowable stress of the wall is exceeded. Also, there is a need to examine the effect that the catalyst type has on the potential for wall damage. Two attempts to mitigate the runaway condition are considered. In addition, two commercial solvers are compared. Lastly, the effect of grid resolution is considered. Table 3 summarizes the cases that are evaluated in the present work. The grey cells mark the issues that have changed from the prior case listed above it. Any case with the recycle "on" is a steady-state case, while those with the recycle shut "off" will be transient cases looking at the potential for thermal damage to the reactor shell. "Normal" catalyst refers to a partially spent catalyst system; "hot" refers to brand new catalyst material. The partially spent catalyst system requires a hotter feed supply to make ample conversion. "N/A" is applied to the bed thermal consideration column for all recycle-on cases, because bed thermal inertia is irrelevant at steady-state. The particular combinations shown in Table 3 were chosen to meet the sponsor's project needs. Cases in groups E and F will be explained in Section 5.3.

4. Methods

4.1. Boundary conditions

Boundary conditions affect CFD results for TBRs (Jiang et al. [6]). Fig. 2 shows the model layout for the geometry for the cases A through D. Although the diameter of the industrial trickle bed reactor is undisclosed, it can be said that it is larger than 1 m. Only 1/16th of the planned reactor is modeled. Since there are no azimuthal gradients in the present work, the case is actually two-dimensional and axi-symmetric. Ansys CFX solver (Section 4.4) does not allow two-dimensional cases to be run, so a finite number of computational cells in the azimuthal dimension are included. Symmetry planes (no normal fluxes) are used for all vertical surfaces at 0° and 22.5° encapsulating the sides of the modeled volume. The catalyst bed has

Table 3
Summary of cases studied.

Case	Solver	Bed thermal	Dim.	Model Geo.	Mesh	Catalyst	Feed disturbance	Feed rate	Recycle
A0	11	N/A	2DA	Bed	Coarse	Normal	Uniform	Normal	On
Al	11	Yes	2DA	Bed	Coarse	Normal	Uniform	Normal	Off
A2	11	Yes	2DA	Bed	Coarse	Normal	Uniform	Reduced	Off
A3	11	Yes	2DA	Bed	Coarse	Normal	Uniform	Off	Off
B0	11	N/A	2DA	Bed	Coarse	Hot	Uniform	Normal	On
Bl	11	Yes	2DA	Bed	Coarse	Hot	Uniform	Normal	Off
B2	11	No	2DA	Bed	Coarse	Hot	Uniform	Normal	Off
C0	11	N/A	2DA	Bed	Coarse	Hot	Center	Normal	On
Cl	11	N/A	2DA	Bed	Fine	Hot	Center	Normal	On
C2	12	N/A	2DA	Bed	Coarse	Hot	Center	Normal	On
D0	11	N/A	2DA	Full	Coarse	Normal	Uniform	Normal	On
E0	12	N/A	3	Bed	Coarse	Normal	Uniform	Normal	On
El	12	N/A	3	Bed	Coarse	Normal	Mal-10	Normal	On
E2	12	N/A	3	Bed	Coarse	Normal	Mal-20	Normal	On
E3	12	N/A	3	Bed	Coarse	Normal	Mal-5	Normal	On
F0	12	N/A	3	Bed	Coarse	Hot	Mal-10	Normal	On

a vapor space above and below it. There is a relatively thick wall at the reactor periphery, called the "shell". The outer surface of the shell is insulated. The liquid (fresh + recycle) and gas are fed in at the top of the TBR and are removed from the bottom. For the "bed" cases, the feeds are placed directly at the top of the bed section; the products are taken directly from the bottom. A bed-only domain not only has fewer computational cells, but it is also much less stiff allowing much larger time steps. These features make a bed-only domain especially attractive for parametric studies. For the non-uniform feed cases, designated "center" in Table 3, liquid is simply jetted down the vessel center region. In all cases an inflow velocity of fluids is used at the inlet, and a zero-gradient condition is used at the outlet. Said boundary conditions are like those presented in Jiang et al. [6].

An unusually simple and coarse mesh with ~2000 hexahedral computational cells is used for most of this effort as designated below the word "coarse" in Fig. 2. The authors are aware of potential gridding issues with CFD results, and more can be found in Strasser et al. [10] and Strasser [11]. As will be shown, increasing the overall cell count by a factor of >5 to the "fine" grid changed the results insignificantly (echoed by the results of Jiang et al. [2]). The lines penetrating the shell and TBR ("S1" and "S2") mark the two locations where probes will be inserted in the operational TBR. They will both be located approximately 50% radially outward from the center. Their heights above the bottom of the bed will be about 0.4 bed diameters (S2) and 1 bed diameter (S1).

4.2. Closing the loop

A form of "process control" methodology is used in the present work to handle the external recycle stream. The exit stream from the bottom of the TBR is conditioned before computationally returning it to the inlet as "recycle". The liquid phase components are space-averaged. The temperature is lowered to the value expected downstream of the recycle cooler. Lastly, the stream is degassed. It is then combined with the fresh feed as discussed previously. Since the recycle composition is so heavily dependent upon the reactor exit composition, the reactor operates in a closed loop mode. In other words, the feed conditions continue to change as the outlet conditions evolve during model convergence in a highly coupled manner. Care is taken to initialize the steady runs with realistic values based on the calibration work, but many iterations are still required to line out the system. Earlier on in the project, before the method had been completely established, various initialization procedures were attempted. There was no evidence of the existence of multiple steady-states.

4.3. Physics approach

An Eulerian–Eulerian multiphase porous media approach is used in the present work. The liquid and gas phases are given independent momentum, mass, energy, and species fields. The bed of catalyst particles is treated as a porous media and is given an independent energy field. Eqs. (2)–(5) show the phasic continuity equation, Reynolds-averaged linear momentum balance in Cartesian coordinates, a species balance, and the energy balance, respectively.

$$\frac{\partial r_\alpha \gamma \rho_\alpha}{\partial t} + \frac{\partial r_\alpha \rho_\alpha K u_{\alpha j}}{\partial x_j} = \gamma S_{\alpha m} + \gamma R_{\alpha l} \tag{2}$$

$$\frac{\partial r_\alpha \gamma \rho_\alpha u_{\alpha i}}{\partial t} + \frac{\partial r_\alpha \rho_\alpha K u_{\alpha i} u_{\alpha j}}{\partial x_j} = \frac{\partial}{\partial x_j} r_\alpha K \times \left[\mu_\alpha \left(\frac{\partial u_{\alpha i}}{\partial x_j} + \frac{\partial u_{\alpha j}}{\partial x_i} - \frac{2}{3}\delta_{ij} \frac{\partial u_{\alpha k}}{\partial x_k} \right) - \rho_\alpha \left\langle u'_{\alpha i} u'_{\alpha j} \right\rangle \right] - r_\alpha \gamma \frac{\partial p}{\partial x_i} + r_\alpha \gamma (\rho_\alpha - \rho_{ref}) g_i + \gamma S_{\alpha m} u_{\alpha i} + \gamma R_{\alpha l} u_{\alpha i} + \gamma M_{\alpha i} - \gamma Z_\alpha \tag{3}$$

$$\frac{\partial r_\alpha \rho_\alpha \gamma \phi_\alpha}{\partial t} + \frac{\partial r_\alpha \rho_\alpha K u_{\alpha j} \phi_\alpha}{\partial x_j} = \frac{\partial}{\partial x_j} r_\alpha K \left[\left(D_\alpha + \frac{\mu_{t,\alpha}}{Sc_{t,\alpha}} \right) \frac{\partial \phi_\alpha}{\partial x_j} \right] + \gamma R_\alpha + \gamma \phi_\alpha S_{\alpha m} \tag{4}$$

$$\frac{\partial r_\alpha \rho_\alpha \gamma C T_\alpha}{\partial t} + \frac{\partial r_\alpha \rho_\alpha C K u_{\alpha j} T_\alpha}{\partial x_j} = \frac{\partial}{\partial x_j} r_\alpha K \left[\left(H_\alpha + \frac{\mu_{t,\alpha}}{Pr_{t,\alpha}} \right) \frac{\partial T_\alpha}{\partial x_j} \right] + \gamma \lambda S_{\alpha m} + \gamma F + \gamma \xi R_{\alpha l} \tag{5}$$

Here, α is a phase designation, γ is the isotropic volume porosity, ρ is the density, λ is the latent heat, ξ is the heat of reaction, Φ is the species mass fraction, μ is the molecular viscosity, and δ is Kronecker delta. Also, K is the isotropic area porosity, M represents interfacial forces (drag and non-drag), p refers to pressure, Pr is the liquid phase Prandtl number, r is the volume fraction of phase α, R is the species reaction rate, S refers to sources for evaporation/condensation, Sc is the Schmidt number, t is for time, T represents static temperature, and u is a velocity (true, not superficial) component. Liquid and gas reaction components are given temperature-dependent properties, including latent heat and vapor pressure. These will remain undisclosed. The liquid phase is incompressible, so the div (normal stress)

can be removed from the right hand side of Eq. (3) for the liquid. Liquid surface phenomena (Surface tension, capillary motion, and wall adhesion) have been excluded from this study, and the catalyst particles are always wetted. Our kinetics rate expressions have particle wetting built in. The basis for R is Eq. (1), which is a strong function of temperature/pressure and is highly exothermic. These temperature-dependent kinetic relationships and temperature-dependent heats of reaction are purposely undisclosed. The gradient diffusion hypothesis has been used to separate the molecular and turbulent diffusive effects on the right hand side of Eqs. (4) and (5). The evaporated and condensed components are incorporated via S. One of the more difficult aspects of this work was the high consumption rate of gas (>95%) via the reaction in Eq. (1). Viscous heating and compression work are ignored in Eq. (5). Note this equation is for each of the fluid phases, without regard to the porous media. One unique feature of the present work is the incorporation of additional sources using FORTRAN that are required in order for the two fluid phases to communicate, thermally, with the porous media. This, in turn, controls the heat up of the entire contents and shell. Without this, there is no thermal inertia of the catalyst particles. Eq. (5), when simplified to remove convective effects, is also used for the reactor wall.

The shear stress transport (SST) k–ω two-equation linear eddy-viscosity model is used for computing the Reynolds stress terms (fluctuating velocity correlations) for the fluid phases and the turbulent contributions in Eqs. (4) and (5). These are necessary to begin to approximate the interphase heat exchange and conjugate heat exchange with the shell. More information on the SST implementation is given by Strasser and Wonders [12]. The difference, however, in present work is that a single homogeneous set of turbulence quantity transport equations is solved for a combined fluid phase. A mixture density and viscosity is used instead the pure phase values. It is well known that eddy-viscosity turbulence computations have limited application even for single phase flows. As with most commercially available Reynolds-averaged turbulence models, for example, the boundary layers are considered everywhere turbulent. Also, there is no turbulence dampening or generation in the porous media. Coupling multiple phase turbulence interactions adds the need for more closures (Strasser [13]). Even though Lopes and Quinta-Ferreira [8] found advantages in the use of the dispersed phase standard k–ε model, this conclusion is expected to depend on the range of length scales and phase volume fractions present. Also, their work did not involve heat transfer, which is the primary purpose for incorporating turbulence models in the present work. For the purposes of industrial parametric HDP reactor evaluations, it was decided the homogeneous SST was a useful starting point.

Eqs. (6) and (7) are used to determine the isotropic porous media momentum sinks.

$$Z_\alpha = \frac{\mu_\alpha}{P} u_{\alpha,\mathrm{mag}} + \frac{I}{2}\rho_\alpha u_{\alpha,\mathrm{mag}}^2 \tag{6}$$

For spherical particles, the isotropic permeability can be estimated by Eq. (7), where d is the catalyst particle mean diameter.

$$P \approx \frac{\gamma^3 d^2}{144(1-\gamma)^2} \tag{7}$$

The basis for liquid–gas mass transfer invoked in the present work is a joint consideration of (1) fluidized bed work of Gao et al. [14], (2) trickle bed work of Larachi et al. [15], and (3) trickle bed work of Wild et al. [16]. The method involves starting with a basic convective mass transfer coefficient relationship for a single phase bed and then modifying it for liquid–gas interfacial interactions. It is assumed, based on the sponsor's experience, that the liquid and vapor remain in near-equilibrium throughout the bed. That means that the mass transfer rates are extremely high, more than an order higher than those predicted using said three approaches of the open literature due to film/droplet condensation effects. In the CFD model, the local rates were effectively increased by an iterative factor until the phases were near equilibrium. As a result of our proprietary conditions, those bases are not shown here. Of course, when mass is moved between phases, the momentum and energy associated with that transport is taken care of via source terms as shown in Eqs. (2)–(5).

For gas–liquid drag, a calibrated Schiller–Naumann [17] type approach is used. A detailed discussion of more in-depth drag relationships are provided by Jiang et al. [6]. Eq. (8) shows the drag coefficient computation, and Eq. (9) shows the Reynolds number basis. The interfacial area available for drag is computed via Eq. (10). Notice, specifically, that the interfacial area is not computed in a fashion that is typical of liquid–gas flows for spherical droplets or bubbles. The shape of the interface is not known at any point in time or space.

$$A = \frac{24}{\mathrm{REGL}}\left(1.0 + 0.15\mathrm{REGL}^{0.687}\right) \tag{8}$$

$$\mathrm{REGL} = \frac{\rho_\mathrm{L} u_{\mathrm{mag,slip}} L}{\mu_\mathrm{L}} \tag{9}$$

$$\theta = \frac{r_\mathrm{L} r_\mathrm{G}}{L} \tag{10}$$

The average length scale, L, is not known a priori. Of course there are a range of length scales present; the reactor is full of catalyst particles in the midst of liquid flowing down in the form of films, drops, and rivulets. Liquid and gas share the space in and around the catalyst particles and vary in space as shown in Lopes and Quinta-Ferreira [1]. A reasonable mean value of L should be at or below the catalyst particle diameter, which is undisclosed. An interfacial length scale ranging from about 1/4th to about 1/10th, depending on the equation, of the catalyst diameter was chosen as starting points. This is reasonable if one considers that catalyst spheres can theoretically pack to a volume fraction of over 70% with all particles touching at their tangents. That leaves little length scale for the gas and liquid rivulets/films to share space.

A Whitaker [18] approach is used for the liquid–gas and fluid–solid heat transfer. The relations for each are similar; the only difference is the particular Reynolds number basis used. In both cases, the liquid phase based Prandtl number is used. GL refers to gas–liquid, while FS refers to fluid–solid.

$$\mathrm{NUGL} = 2 + \left(0.4\mathrm{REGL}^{0.5} + 0.06\mathrm{REGL}^{2/3}\right) Pr^{0.4} \tag{11}$$

$$\mathrm{NUFS} = 2 + \left(0.4\mathrm{REFS}^{0.5} + 0.06\mathrm{REFS}^{2/3}\right) Pr^{0.4} \tag{12}$$

$$\mathrm{REFS} = \frac{\rho_\mathrm{L} u_{\mathrm{L,mag}} d}{\mu_\mathrm{L}} \tag{13}$$

There is no current implementation of transient fluid–solid heat transfer to a porous media in either of ANSYS' family of commercial CFD codes (Fluent and CFX). FORTRAN must be used to incorporate catalyst thermal inertia, so a code was devised that communicates Eqs. (12) and (13) between the Eulerian–Eulerian phases and the porous media. The FORTRAN code was validated by comparing a simple CFX test case with that of a known solution involving Bessel functions. It should be noted here that since the catalyst particles only touch at the corners, there is a reduced thermal conductivity associated with the bulk porous phase.

The interior wall between the fluids and reactor wall is a 1:1 interface, meaning the nodes on the solid side line up perfectly with those on the TBR side. Heat is communicated by both conduction and convection on the TBR side and conduction on the wall side. The conduction is straight forward, while the convection relies on a typical heat transfer coefficient found by the solver as outlined in the ANSYS solver documentation [19]. Near-wall turbulence from the SST model sets the wall profiles which control the local heat

convective rates. Of course, this is only an approximation since the turbulence length scales present are complex and unknown.

4.4. Numerics

Eqs. (2)–(5) are discretized and solved using a commercial ANSYS double precision unstructured solver. Two solver versions are considered here, CFX version 11 with service pack 1 and CFX version 12. These are noted "11" and "12" in Table 3. Both CFX versions utilize a vertex-based finite volume method in which each term is converted to mesh element volume integrals and element surface integrals. A high resolution algorithm similar to that of Barth and Jesperson [20] is used to discretize advection terms. Time derivatives are discretized using a first order transient scheme. This first order temporal scheme injects minimal error into the solution due to the extremely small time step that had to be used, which will be addressed more in Section 4.5. Mass flows are discretized using a Rhie–Chow approach (modified by Majumdar [21]), to avoid pressure decoupling on the co-located grid. Newton–Raphson linearization addresses compressibility effects. Viscous stresses, diffusion terms, and the pressure gradient are discretized using typical finite element shape functions. These shape functions depend on the mesh element type. Velocity and pressure are coupled together in the same matrix, making the solution algorithm fully implicit. Finally, a coupled ILU algebraic multigrid technique is used to solve the resulting system of matrices.

4.5. Convergence

All simulations are run as transient to help in convergence, as the highly coupled nature of this work makes CFD relatively stiff. A very small time step relative to the main measured variable (thermal response) is required. The ratio of typical time step size to the time required for the bed temperature to reach a new steady-state is approximately O (1:100,000). Each steady-state feed case is run until important measures, such as temperature and velocity at monitoring points and overall conversion, are not changing to four significant figures. RMS residuals are all normally less than 10^{-10} when this occurs. Transient feed cases are converged within each time step to the point at which RMS residuals are all less than 10^{-7}, normally requiring 8 to 10 inner loops within the time step. Unsteady runs took between 1 and 3 weeks, depending on much flow time was needed to assess the temperature rise, on an HP-XW8400 machine with a Dual Core Intel 5260 CPU using windows XP-64. Given the time required to converge on a relatively coarse and simple mesh, the individual particle method of Lopes and Quinta-Ferreira [1] would have required cost-prohibitive modeling times for our sponsor. More about transient CFD statistics and convergence monitoring strategies can be found in Strasser [22].

4.6. Calibration

A stepwise calibration effort was undertaken in order to establish the basis for the porous media resistance as shown in Eq. (6). First, a liquid-only case was run. The permeability is given by Eq. (7), so the inertial resistance factor, I, was modified until the bed pressure drop matched the well-known Ergun relationship. Next, gas-only cases were run in a similar manner. It was found that nothing had to be changed to make a gas-phase match. This makes sense, considering the Ergun relationship is not phase-dependent. Then, both phases were included in a "cold flow" model with uniform feed, no reactions, no heat transfer, no mass transfer, and volume-averaged phase properties. In the LIR, liquid–gas interfacial effects are real (albeit small), so it is expected that the losses will not be the same as single phase runs. The Larachi [15] correlations from Al-Dahhan et al. [3] should best represent the pressure drop and liquid phase holdup of the present work, so Eq. (6) was modified until the cold flow test case matched the pressure drop and holdup of Larachi et al. [15] to within 3%. The resistances were modified in a "relative permeability" style approach (Nemec and Levec [23]) until the multiphase flow resistance was about 1.5 times that of the liquid-only flow and about 6200 times that of the gas-only flow, which are reasonable according to said work. Note that a different choice of mean length scale L might result in a different calibration result. Clearly the momentum balance at the computational cell level is compilation of multiple effects and can be arrived at from multiple directions (Strasser and Wonders [12]). Lastly, case A0 (all kinetics, CHT, gas consumption, etc. added in) was ran and was found to match the sponsor's models based on plant data. The CFD model matched conversion, component flows, and outlet temperature to within 4% as shown in Table 4. Future work should include testing the sensitivity of the results to various values of the characteristic length scale.

Table 4
Comparison of sponsor data and CFD case A0 calibration results.

	AO, sample 1 %Error	AO, sample 2 %Error
Liquid flow	−0.23	−0.14
Vapor flow	2.48	4.00
Reactant A in liquid	−1.82	−1.82
Reactant B in liquid	0.08	0.08
Reactant C in liquid	−0.08	−0.08
Reactant A in vapor	−3.92	−2.10
Reactant B in vapor	3.50	1.87
Temperature	0.24	0.24
Pressure	0.03	0.03

5. Results and discussion

5.1. 2-D axi-symmetric steady flow cases (recycle on)

Fig. 3 shows the steady-state liquid phase holdup profiles for all the steady-state cases shown in Table 3. In all cases, the values shown represent area-averages (with mass-flow weighting) at bed cross-cuts starting at the top and moving down the reactor. 0.0 would be the top of the catalyst bed, while 1.0 would be the bottom of the catalyst bed. The bed height is between 1 and 2 bed diameters, while the entrance length is more than a bed diameter. Also, in all cases, the holdup values have been normalized by each particular bed volume average. It can be seen that all of the profile are relatively axially flat. This is expected in that the bed resistance is

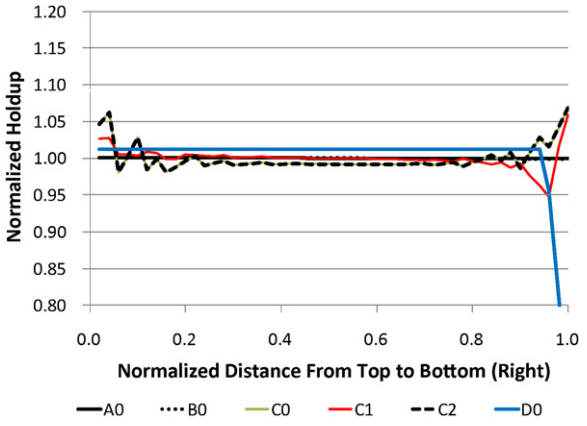

Fig. 3. Holdup profiles for all steady cases. Axial holdup values have been normalized by the bed volume average.

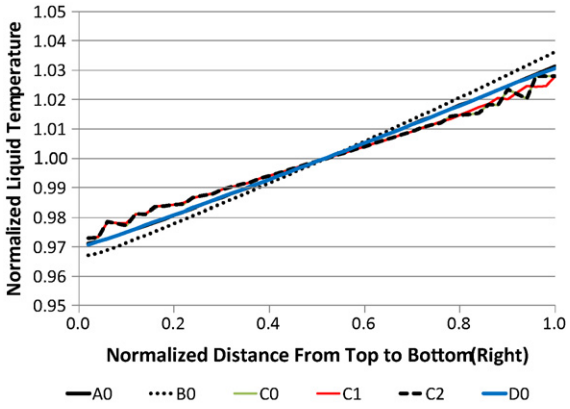

Fig. 4. Liquid temperature profiles for all steady cases. Axial temperature values have been normalized by the bed volume average.

isotropic. The mal-distributed cases have a slight parabolic nature. Comparing C0, C1, and C2 reveals that grid refinement and solver change have little effect; the refined grid case does have a smoother holdup profile than the coarse cases and a dip near the bottom. There is some indication that the lower section of the bed is sensitive to how far it is from the modeled "outlet". The D0 case (vapor space above and below the bed) appears to lose some holdup at its bottom, while the others (with outlets coinciding with the bottoms of the beds) do not. Catalyst type has no detectable effect.

Axial normalized liquid temperature profiles for all steady cases are shown in Fig. 4. As with Fig. 3, the values are planar averages that have been normalized by the bed volume average. Since the bed is at steady-state and thermal equilibrium, the gas, bed particles, and shell temperature profiles match the liquid. The normalized values in the figure are somewhat insensitive to all factors tested. They all show a slight heating trend, which makes sense given the exothermic nature of the reaction. Again, grid resolution and a solver change have little impact. There is a minor profile smoothing effect by increased grid resolution. Hotter catalyst shows a slightly steeper trend, which would be expected. Mal-distribution causes a less aggressive trend since there is less volume utilized for reaction.

Fig. 5 gives axial profiles for normalized values for an important reactant. All show a generally falling trend, which make sense in a reactive system. Each of the three mal-distributed cases (C0–C2) shows a weaker trend than the uniform feed cases. This is a result of reduced volume available for reaction in the bed. Again, the solver or grid refinement issues do not appear to matter much. Although the grid showed the aforementioned small holdup effect, the holdup effect does not translate through to the reactant concentration. The only noticeable effect is a slight smoothing of the profile.

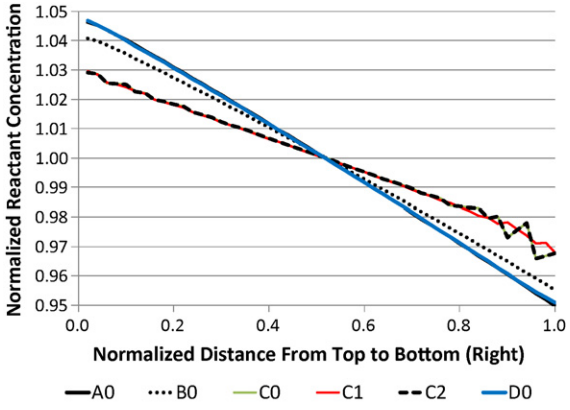

Fig. 5. Reactant concentration profiles for all steady cases. Axial concentration values have been normalized by the bed volume average.

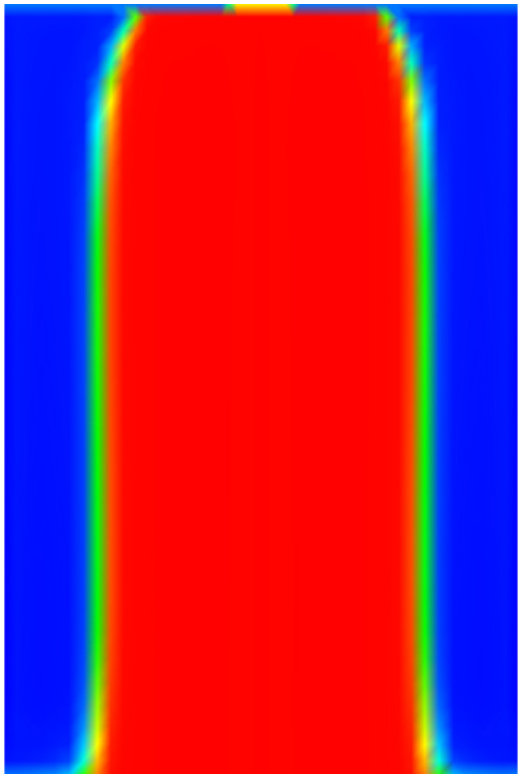

Fig. 6. Liquid holdup in case C1.

For further insight, Fig. 6 is included to show the liquid mal-distribution in the bed for the "C" cases. The color scale is linearly ranged between 0.41 (blue) and 2.0 (red) times the volume mean liquid holdup. The picture in Fig. 6 has been mirrored about the bed axis for visual assistance. The small jet can be seen entering the top and is quickly diffused radially outward by the catalyst particles. The spreading rate will likely be a strong function of bed resistance parameters and other issues with the momentum balance. Further research is required to assess the effect of this on conversion. A large portion of the reactor is not being utilized by the reaction medium (liquid), which is the reason for the lower conversion in upcoming Table 7. For steady-state cases A0, B0, and D0, there is no radial variation in any computed property, so those contours have not been included here. Also included for interest is liquid temperature contours in the reactor shown in Fig. 7. The color scale is linearly ranged between 0.75 (blue) and 0.86 (red) for temperature normalized by the failure temperature. Two conclusions can be made. First, the temperatures are not radially uniform from top to bottom like the other cases are. The temperature is higher out near the bottom periphery where the liquid holdup is low. There is just enough liquid there to encourage reactions (and temperature escalation), but not enough to keep the areas cool. Second, there is very little effect of >5× increased grid resolution. The contours for case C0 are very similar in shape to those in C1. To a very small degree, however, the temperatures in C1 are higher in value, lower in the reactor, and encompass more material radially.

In summary axial temperature, holdup, and reactant concentration are fairly insensitive to (1) catalyst type/reactivity, (2) solver type, (3) grid resolution, and (4) modeled domain extent when the respective planar averages are normalized by each bed volume average. Obviously, said normalization process desensitizes the results, to some extent, to changes in these four features. Even beyond that, one might conclude these findings are logical. Catalyst

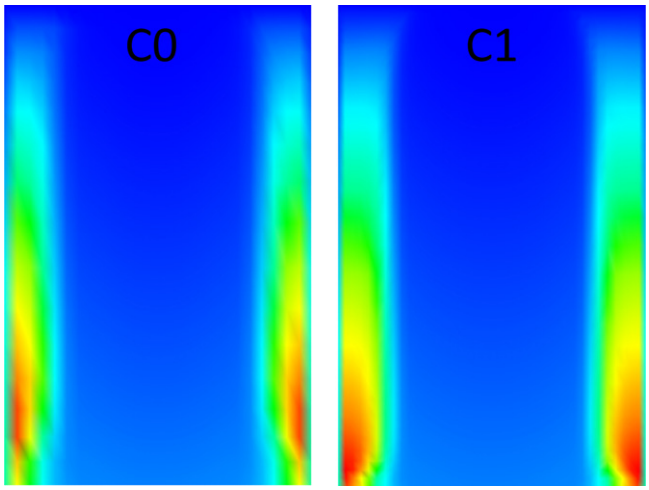

Fig. 7. Liquid temperature in cases C0 and C1.

reactivity is not a strong player due to how the real plant process is normally operated; as previously mentioned, feed temperature is reduced for fresh catalyst to keep a similar overall conversion. The particular solver version (CFX 11 versus CFX 12) did not affect the axial values much in that there were no major changes to the solver's E–E approach between the two releases. The lack of grid resolution sensitivity points to the fact that the spatial gradients in the present work are resolved well enough with the initial grid. Lastly, the modeled domain extent (bed, inlet, and outlet versus bed-only) would not be expected to contribute much to the results, because there are little to no sources, sinks, or gradients in the plant process above or below the bed.

5.2. 2-D axi-symmetric transient flow cases (recycle loss)

Again, the purpose of the transient studies is to determine how long it takes for the temperatures to reach some critical value, designated Tfa. It should be clarified that the term "failure" is used to loosely refer to a condition which could exceed a predetermined safe operating value for the reactor shell metal. Two methods of minimizing the temperature derivative are evaluated. The first of these methods is to reduce the fresh reactant feed to a value of ~20% of the typical feed value. The other is to cut the feed to about 20% of the typical for some time and then shut it off completely. Cases A1 and B1 are cases in which recycle is lost, and nothing is done to mitigate the heating. Case A2 involves reducing the feed value and holding it. Case A3 involves a reduce-then-off feed method. B2 is similar to B1, except that the FORTRAN has been removed to assess the importance of catalyst particle thermal inertia.

Figs. 8–10 show all transient response curves at probe S1, S2, and the wall peak value, respectively. The wall peak value refers to the highest temperature reached anywhere on the inner shell wall, regardless of where it occurs. Absolute temperatures have been normalized by Tfa on all these plots. In general S2 responds more slowly than S1 (higher in the reactor) and more quickly than the wall value. Compared to A1, B1 rises in a similar fashion even though the B1 catalyst is hotter. As alluded to in Section 3, the "normal" catalyst requires a higher feed temperature than the "hot" catalyst in order to produce an acceptable conversion. Apparently, the hotter catalyst effects are offset by the cooler feed effects during these transient responses. A2 takes much longer than A1, indicating that the reduced feed mitigation method is very useful. A3 is much slower than any of them, which says that completely shutting off the feed is much more powerful at reducing the heating rate. If the catalyst thermal inertia is ignored (case B2 versus B1), the system

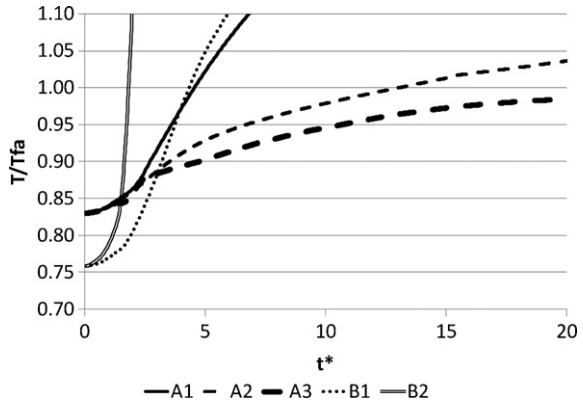

Fig. 8. All S1 response curves.

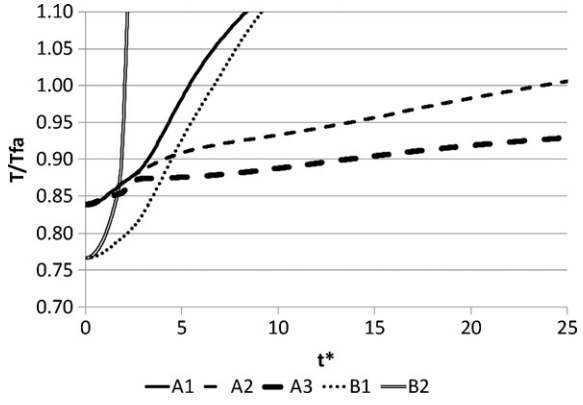

Fig. 9. All S2 response curves.

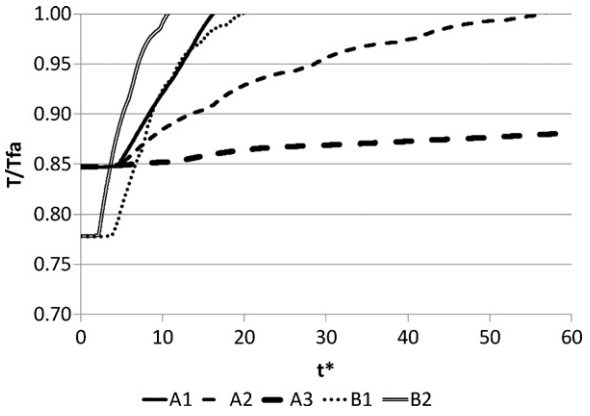

Fig. 10. All shell inner temperature peak response curves.

temperature rise is dramatically higher; therefore, it is important to include said effect.

Table 5 includes the quantification of Fig. 10. It shows the duration, in residence times, from the time the recycle is shut off until

Table 5
Summary of time for wall peak to reach Tfa.

Case	Mitigation method	t^* to Tfa
Al	None	16
A2	Reduce feed	57
A3	Feed off	>100
Bl	None	20
B2	None	11

*Normalized by residence time.

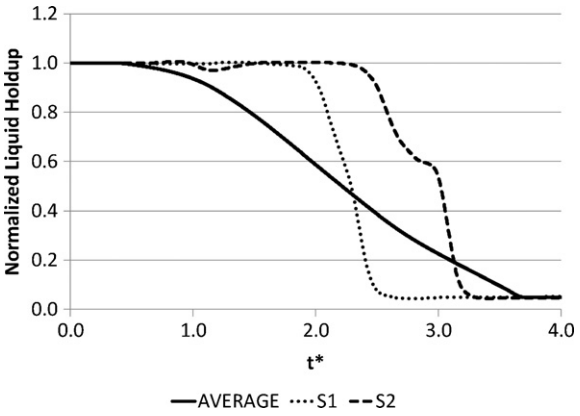

Fig. 11. Transient holdup response for case A1.

the point at which the wall reaches the critical value. B1 is similar to A1, but is slightly slower. This indicates that the B1 cooler feed more than compensates for the B1 hotter catalyst. The first mitigation method is valuable at slowing the rise (more than a factor of 3). The exact relative effect of the mitigation method is unknown. The sponsor did not want to run A3 long enough to find the time required to reach the critical value. It can be said that the A3 wall peak was only 90% of the critical value at 100 residence times. As previously discussed, when the thermal inertia of the solid bed is ignored, the bed heats in about half the time (11 residence times versus 20).

Fig. 11 shows liquid holdup responses for case B1 at S1, S2, and the bed average. All values are normalized by the starting bed average. In the real plant, there will not be any volume fraction probes at any point in the vessel; these results are provided to assess spatial variation. The emptying of the reactor is clearly seen in the plot. The average starts to fall immediately, while S1 takes time to respond, followed by S2. The bed appears to be completely empty in less than four residence times. Notice, however, that it does not go completely empty. That is because the fresh feed is still moving into the vessel; only the recycle (large fraction of the total) has been shut off.

5.3. 3-D steady flow cases (recycle on)

The final type of model to be discussed involves cases E–F in which the mal-distribution is three-dimensional in nature. Instead of jetting most of the liquid down the centerline as in the 2-D cases in Section 5.1, there is a region occupying about a third of the reactor where a failing distributor is considered as shown in Fig. 12. The plane of symmetry augmented the study by allowing only a half

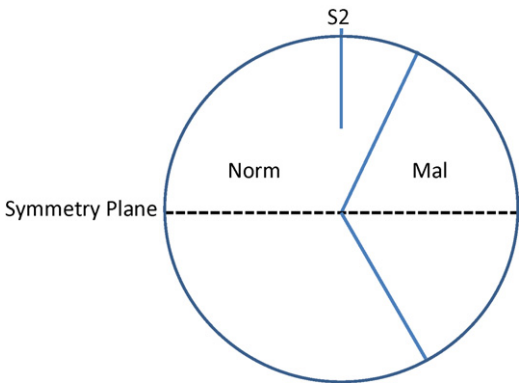

Fig. 12. Layout of 3-D model.

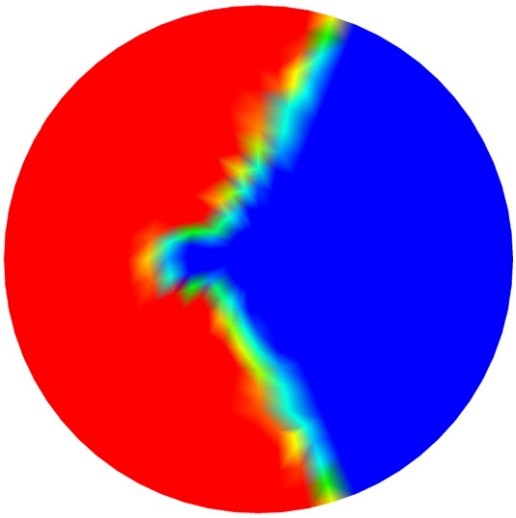

Fig. 13. Liquid holdup for E3 on an axial mid plane.

reactor to be studied each time. As shown in Table 3, there are four permutations considered. The first three are with the normal catalyst, while the last one is with the hot catalyst. The variant between the first three is the amount of liquid feed to the mal-distribution sector. “Mal-10”, for example, implies that only 10% of the normal liquid flow is sent to the sector involving the faulty distributor.

Cross-sectional liquid holdup (plan view) is shown in Fig. 13 for a plane mid-way through the catalyst bed for case E3. The color scale is linearly ranged between 0.21 (blue) and 1.1 (red) times the volume mean liquid holdup. The inclusion of only 5% of the normal flow to the mal-distributed sector has a clear effect throughout the reactor. Fig. 14 shows the cross-sectional liquid temperature at the same location with ranges undisclosed. The material gets progressively hotter approaching the wall where there exists enough liquid to allow reaction to proceed without effective cooling. Elevation view of cross-sectional liquid temperature is depicted in Fig. 15. The material is indeed hotter near the wall, but closer to the top than was shown earlier in Fig. 7. The color scales in Figs. 14 and 15 are linearly ranged between 0.82 (blue) and 0.99 (red) for temperature normalized by the failure temperature. It is evident that the type and extent of the feed mal-distribution is important to the generation of hot-spots. Lopes and Quinta-Ferreira [1] showed

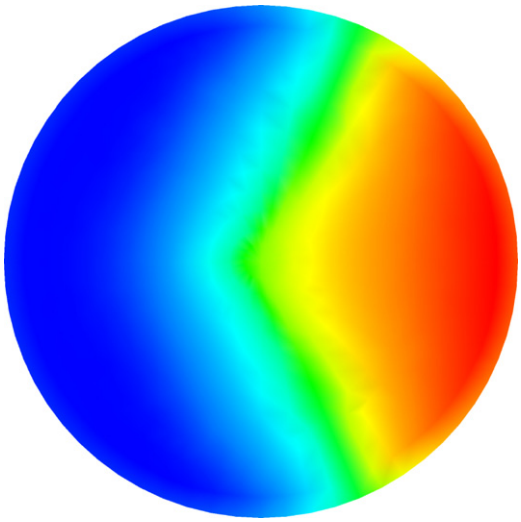

Fig. 14. Liquid temperature for E3 on an axial mid plane.

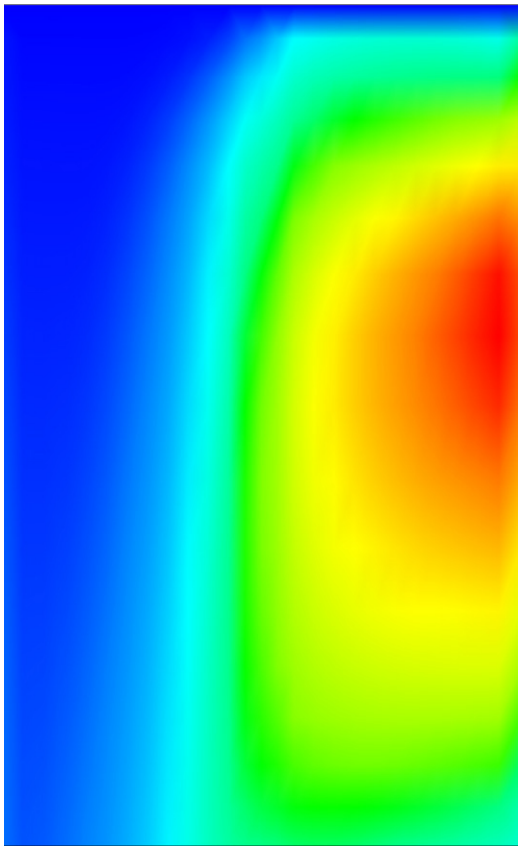

Fig. 15. Liquid temperature for E3 on the symmetry plane.

that hot-spot potential depended on phase distribution. Although their study involved a uniform feed system, their individual catalyst particles modeling approach allowed for more precise spatial phase resolution than can be provided here. They showed that, even for a supposedly uniform feed, catalyst underutilization can occur throughout the reactor.

Table 6 illustrates the liquid temperature gradient increase as a result of the mal-distributed feed systems considered in the present work. The values are normalized by subtracting each result by the outlet value and help to give quantification to the previously discussed figures. A number of comparisons can be made from this table. First, for the axi-symmetric cases A–C, it can be seen that S1 and S2 are typically lower than the outlet value. This corresponds to axial bed heating as expected and as shown in Fig. 4. Also, the peak wall inner value is normally higher than the outlet. The expected result of mal-distribution (C0 versus B0) is an increase in the internal gradients; the peak wall value is much higher in the case of the faulty feed system. Also, S1 and S2 deviate more from the outlet

Table 6
Some normalized liquid temperature point gradients.

Case	Temperatures		
	Peak	S1	S2
A0	1	−10	−4
B0	2	−9	−4
C0	13	−12	−9
E0	1	−10	−5
El	84	7	16
E2	77	−1	12
E3	70	9	14
F0	73	0	9

Table 7
Summary of normalized steady-state conversions.

Case	Feed distribution	Normalized steady-state conversion
A0	Uniform	1.00
B0	Uniform	1.00
C0	Center	0.83
Cl	Center	0.83
C2	Center	0.83
D0	Uniform	1.00
E0	Uniform	1.00
El	Mal-10	1.04
E2	Mal-20	1.06
E3	Mal-5	0.96
F0	Mal-10	1.09

values in case C0 compared to B0. The values for C1 are not shown here, as they are not much different from C0. Case E0 looks very similar to A0 and should in that the only difference is the modeled dimension. For the 3-D mal-distribution cases, where the dry areas are a much larger fraction of the bed, we see the situation much more exacerbated (Fig. 15 versus Fig. 7). The wall peaks are much higher in the 3-D cases. S1 and S2 see changes caused by distribution, but not as much as the wall peaks. That is a result of the fact that the probes are not in the faulty sector. It can also be seen that peak value is not a monotonic function of % feed lost in the sector. E3, while having worse distribution, does not have as much of a gradient as E1. As indicated previously, it is the presence of some liquid (without enough to convectively cool) that creates the worst hot-spots.

One important element of the present study which needs more attention is the overall productivity, or conversion, of the reactor under the studied conditions. In Fig. 5, each reactant concentration profile is normalized by its respective volume average. As a result, it is not obvious which case is capable of more production than the other. To clarify, Table 7 is offered as a summary of relative overall reactor conversions. It can be seen that mal-distribution in the 2DA cases results in an overall reduction in conversion by about 20%. It can also be seen that solver choice and grid refinement made very little difference as with previous plots. Whether a full reactor or just a catalyst bed is modeled (A0 versus D0) appears to have almost no effect on overall steady-state conversion.

Apparently, the very high temperatures caused by the 3-D mal-distribution cases convert enough material to partially offset the effect of the lower volumetric catalyst utilization. It is not proposed that this is a positive situation, but the effect on overall conversion seems to depend on the type and extent of spatial feed problem situation. In fact, some cases actually show increased overall conversion due to the extremely elevated temperatures. It is likely that our kinetic relationships are not valid at these high temperatures, so we realize this is just an approximation. It should be noted again that Fig. 6 shows a very fast radial dispersion of the feed jet to the inlet center cells (similar to the point source method of Lappalainen et al. [9]). Not only are there many uncertainties surrounding turbulence modeling in this situation, but also we have ignored liquid surface phenomena (surface tension, capillary motion, and wall adhesion). Jiang et al. [6] propose that the Reynolds stress term is not important in determining the macro-scale flow pattern in packed beds with a particle size of 10^{-4} to 10^{-2} (current work in this range). Perhaps future work could include more evaluations to study how these parameters and spreading rates affect conversion. In addition, a spatial porosity variation could be easily included in the CFD method to incorporate potentially important effects as described in Lappalainen et al. [9] and Jiang et al. [6].

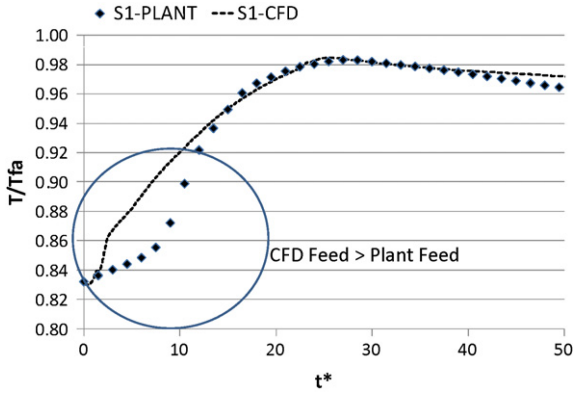

Fig. 16. Thermal response of CFD versus the plant.

5.4. Plant comparison of potential runaway

Months after the aforementioned computational work was completed, the reactor unit was constructed, installed, and started. An unplanned loss in plant recycle flow was experienced, and limited data were collected. The A3 style mitigation method was employed; that is, the fresh reactant feed was set to shut off after the recycle flow was lost. There are differences in how, precisely, mitigation was handled in the plant versus how mitigation was modeled in CFD a priori. In CFD, the A3 fresh feed was reduced to a very low amount, linearly in two stages over the first ~19 time units. In the plant incident, however, the fresh feed was shut off nearly immediately, or as fast as measurement devices could detect. The fresh feed provides the reactants, so it is the primary energy input into the system. The thermal response in the plant should be less potent at the onset compared to CFD, since the plant had a more quickly shut off of the fresh feed. Fig. 16 shows the response of CFD compared with the plant. The CFD shows more of an increase in the beginning due to the differences in the feed shutdown methods, as noted on the plot. Both S1 curves reach approximately the same maximum. Plant engineers used the CFD model to establish other control strategies (on variables not discussed here) before the plant start-up. Since S1 responded with approximately the same peak, plant personnel knew they had correct strategies in place. In addition, the new reactor's dynamic holdup was found to be 33%, while CFD predicted 35%. Detailed data are not available to compare the plant draining during the excursion to those results in Fig. 11, but coarse plant level measurements show that the majority of the liquid drains from the bed in a few residence times. Obviously, the CFD response would have been far too fast without the catalyst thermal inertia. It was concluded that the current CFD method offers a reasonable design tool.

6. Conclusions

A multi-faceted CFD study was carried out involving an HDP trickle bed reactor with high mass transfer rates, a large fraction (>95%) of the incoming gas consumed by the reaction, and an external closed loop recycle stream. Hydrodynamics were strongly coupled with kinetics and mass transfer. Steady-state and transient cases were considered in order to study the effects of feed distribution, catalyst system, and thermal runaway. FORTRAN code had to be involved to take care of the transient sensible heat communication between the Eulerian–Eulerian fluid phases with the porous catalyst phase. Before proceeding to study various configurations, a stepwise calibration process was undertaken. Calibration involved tuning the porous resistances, first using individual phase flows across the bed, and then both phases at average flow conditions to tune gas–liquid interfacial effects. Lastly, the fully reactive system was matched to the sponsor's calculations. Two-dimensional and three-dimensional mal-distribution cases were studied, showing that the effect of feed distribution on overall conversion depends on the extent of the mal-distribution. Two-dimensional recycle stream interruption studies were undertaken in order to assess the potential for thermal runaway and how to minimize its extent. The following conclusions can be drawn from this study:

1. Axial temperature, holdup, and reactant concentration, when normalized by their respective bed volume averages, are fairly insensitive to catalyst type, solver type, grid resolution, and modeled domain extent.
2. A faulty feed distributor which jets the liquid down the vessel centerline can cost about 20% in overall reactor productivity, but the effect on conversion depends on the type and extent of mal-distribution.
3. Feed distribution method, and to a lesser extent grid resolution, do affect the radial profile of important results in the reactor.
4. The inclusion of the solid catalyst bed particles thermal inertia via FORTRAN accounts for an important thermal transient. Without this effect a thermal runaway condition can become problematic in about half the time computed from the more rigorous method.
5. The potential for a thermal problem does not appear to be necessarily linked to the strength of the catalyst activity, assuming feed temperatures are adjusted accordingly for catalyst activity during normal operation.
6. Reducing the reactor feed in the event the cooling recycle stream is lost can be an effective method in increasing the runaway heat up delay.
7. A bed-only CFD model, which ignores the computational vapor space above and below the catalyst bed particles, can be an effective tool for trickle bed reactor studies.
8. CFD results compared well with plant data in regards to holdup, drain time, and thermal response.

Acknowledgements

The author would like to express gratitude to Kurt Svihla of ANSYS, Inc. who wrote the FORTRAN code for this work.

References

[1] R. Lopes, R. Quinta-Ferreira, Evaluation of multiphase CFD models in gas–liquid packed-bed reactors for water pollution abatement, Chemical Engineering Science 65 (2010) 291–297.
[2] P.R. Gunjal, V.V. Ranade, Modeling of laboratory and commercial scale hydroprocessing reactors using CFD, Chemical Engineering Science 62 (2007) 5512–5526.
[3] M.H. Al-Dahhan, F. Larachi, M.P. Dudukovic, A. Laurent, High-pressure trickle-bed reactors: a review, Industrial and Engineering Chemistry Research 36 (1997) 3292–3314.
[4] J. Charpentier, M. Favier, Some liquid hold-up experimental data in trickle bed reactors for foaming and nonfoaming hydrocarbons, AIChE Journal 21 (1975) 1213–1218.
[5] Y. Jiang, M. Khadilkar, M. Al-Dahhan, M. Dudukovic, CFD modeling of multiphase flow distribution in catalytic packed bed reactors: scale down issues, Catalysis Today 66 (2001) 209–218.
[6] Y. Jiang, M. Khadilkar, M. Al-Dahhan, M. Dudukovic, CFD of multiphase flow in packed-bed reactors: I. k-Fluid modeling issues, AIChE Journal 48 (2002) 701–715.
[7] R. Lopes, R. Quinta-Ferreira, Trickle-bed CFD studies in the catalytic wet oxidation of phenolic acids, Chemical Engineering Science 62 (2007) 7045–7052.
[8] R. Lopes, R. Quinta-Ferreira, Turbulence modeling of multiphase flow in high-pressure trickle-bed reactors, Chemical Engineering Science 65 (2009) 291–297.
[9] K. Lappalainen, M. Manninen, V. Alopaeus, CFD modeling of radial spreading of flow in trickle-bed reactors due to mechanical and capillary dispersion, Chemical Engineering Science 64 (2009) 207–218.
[10] W. Strasser, G. Feldman, C. Wilkins, J. Leylek, Transonic passage turbine blade tip clearance with scalloped shroud: Part II – losses with and without scrubbing effects in engine configuration, ASME Paper No. IMECE2004-59116.

[11] W. Strasser, CFD investigation of gear pump mixing using deforming/agglomerating mesh, Journal of Fluids Engineering 129 (2007) 476–484.
[12] W. Strasser, A. Wonders, Commercial scale slurry bubble column reactor optimization, WIT Transactions on Engineering Sciences 59 (2008) 275–287.
[13] W. Strasser, Discrete particle study of turbulence coupling in a confined jet gas–liquid separator, Journal of Fluids Engineering 130 (2008) 1–11.
[14] J. Gao, J. Chang, X. Lan, Y. Yang, C. Lu, X. Chunming, CFD modeling of mass transfer and stripping efficiency in FCCU strippers, AIChE Journal 54 (2008) 1164–1177.
[15] F. Larachi, A. Laurent, N. Midoux, G. Wild, Experimental study of a trickle-bed reactor operating at high pressure: two-phase pressure drop and liquid saturation, Chemical Engineering Science 46 (1991) 1233–1246.
[16] G. Wild, F. Larachi, J. Charpentier, Heat and mass transfer in gas–liquid–solid fixed bed reactors, Heat and Mass Transfer in Porous Media, Elsevier, Amsterdam (1992) 616.
[17] L. Schiller, Z. Naumann, A drag coefficient correlation, Zeitschrift fur Vergleichende 77 (1935) 318.
[18] S. Whitaker, Forced convection heat transfer correlation for flow in pipes, past flat plates, single cylinders, single spheres and flow in packed beds and tube bundles, AIChE Journal 18 (1972) 361–371.
[19] ANSYS Solver Documentation, 2009.
[20] T. Barth, D. Jesperson, The design and application of upwind schemes on unstructured meshes, AAIA Paper 89-0366 (1989).
[21] S. Majumdar, The role of underrelaxation in momentum interpolation for calculation of flow with nonstaggered grids, Numerical Heat Transfer 13 (1988) 125–132.
[22] W. Strasser, Cyclone-ejector coupling and optimization, Progress in Computational Fluid Dynamics 10 (2010) 19–31.
[23] D. Nemec, J. Levec, Flow through packed bed reactors: 2. Two-phase concurrent downflow, Chemical Engineering Science 60 (2005) 6958–6970.